

Article

Effect of La and Sc Co-Addition on the Mechanical Properties and Thermal Conductivity of As-Cast Al-4.8% Cu Alloys

Zhao-Xi Song¹, Yuan-Dong Li^{1,2,*} , Wen-Jing Liu¹, Hao-Kun Yang¹, Yang-Jing Cao¹ and Guang-Li Bi^{1,2}

- ¹ State Key Laboratory of Advanced Processing and Recycling of Nonferrous Metals, Lanzhou University of Technology, Lanzhou 730050, China; lionel_xi@163.com (Z.-X.S.); wenjing_liu133@163.com (W.-J.L.); yanghk_0123@163.com (H.-K.Y.); yangjing_cao@163.com (Y.-J.C.); glbi@163.com (G.-L.B.)
- ² Key Laboratory of Non-Ferrous Metal Alloys and Processing, Ministry of Education, Lanzhou University of Technology, Lanzhou 730050, China
- * Correspondence: liyd@lut.cn; Tel.: +86-931-297-6795

Abstract: The effects of La and La+Sc addition on mechanical properties and thermal conductivity of Al-4.8Cu alloy were comprehensively studied. The as-cast samples were characterized by optical microscopy (OM), scanning electron microscopy (SEM), X-ray diffraction (XRD) and first-principles methods. The results reveal that the grain morphology of Al-4.8Cu alloy changes from dendrite to fine equiaxed grain with La, La+Sc addition. The average grain size of Al-Cu-La (Al-4.8Cu-0.4La) and Al-Cu-La-Sc (Al-4.8Cu-0.4La-0.4Sc) decreased by 37.2% (70.36 μm) and 63.3% (119.64 μm) respectively compared with Al-Cu (Al-4.8Cu). Al-Cu-La has the highest elongation among the three which is 34.4% (2.65%) higher than Al-Cu. Al-Cu-La-Sc has the highest ultimate tensile strength and yield strength which are 55.1% (80.9 MPa) and 65.2% (62.1 MPa) higher than Al-Cu, respectively. The thermal conductivity of Al-Cu-La and Al-Cu-La-Sc is 10.0% (18.797 $\text{W}\cdot\text{m}^{-1}\cdot\text{k}^{-1}$) and 6.5% (12.178 $\text{W}\cdot\text{m}^{-1}\cdot\text{k}^{-1}$) higher than Al-Cu alloy respectively. Compared with Al-Cu, Al-Cu-La has less shrinkage and porosity, the presence of Al_4La and AlCu_3 contribute a lot to the decrease of specific heat capacity and the increase of plasticity and toughness. The porosity of Al-Cu-La-Sc does not significantly decrease compared with Al-Cu-La, the presence of Al_3Sc and AlCuSc bring about the increase of specific heat capacity and brittleness.

Keywords: Al-Cu alloy; microstructure; mechanical properties; thermal conductivity; first-principles



Citation: Song, Z.-X.; Li, Y.-D.; Liu, W.-J.; Yang, H.-K.; Cao, Y.-J.; Bi, G.-L. Effect of La and Sc Co-Addition on the Mechanical Properties and Thermal Conductivity of As-Cast Al-4.8% Cu Alloys. *Metals* **2021**, *11*, 1866. <https://doi.org/10.3390/met11111866>

Academic Editor: Daixiu Wei

Received: 20 October 2021
Accepted: 16 November 2021
Published: 20 November 2021

Publisher's Note: MDPI stays neutral with regard to jurisdictional claims in published maps and institutional affiliations.



Copyright: © 2021 by the authors. Licensee MDPI, Basel, Switzerland. This article is an open access article distributed under the terms and conditions of the Creative Commons Attribution (CC BY) license (<https://creativecommons.org/licenses/by/4.0/>).

1. Introduction

Since miniaturization and integration are always the evolution trend of electronic components and power output devices, the influence of high-temperature environment formed by local heat concentration on the stability of semiconductor components and structural parts will be inevitable [1–3]. Many studies have shown that the working stability of electronic components will decrease with the increase of temperature, and the failure probability increases exponentially with the temperature increase [4,5]. Also, the formation of thermally induced stresses and mechanical harmful hot-spot defects will be easier [6]. Therefore, the research of materials with high thermal conductivity will run through the process of scientific and technological development.

Aluminum alloys are widely used in the aviation, automobile and electronic information industry due to the low cost, low density and high specific strength [7,8]. Al-Cu alloys have better casting performance and higher thermal conductivity than Al-Zn-Mg-Cu alloys, and higher yield strength than Al-Mg-Si traditional high thermal conductivity alloys. Notwithstanding the thermal conductivity of pure Al is $237 \text{ W}\cdot\text{m}^{-1}\cdot\text{k}^{-1}$, elements added to the Al matrix to improve the mechanical properties, such as Si, Cu, Zn, Mg, etc. will reduce it [9].

Due to the high chemical activity, low potential and unique electronic shell structure of rare earth elements such as Sr, La, Ce, Er and Sc, they are often used as micro-alloying

elements to optimize the structure and properties of alloys [10]. Zheng et al. [11] found that although adding La to Al-Mg-Si alloy does not change the precipitation sequence and the atomic structure of the precipitates, it can decrease the solubility of Si and Mg in the Al matrix and the precipitation activation energy of β'' . This leads to the simultaneous improvement of the strength and electrical conductivity of the Al-Mg-Si alloy. Du et al. [12] reported that Ce promotes the formation of the $\text{Al}_8\text{Cu}_4\text{Ce}$ phase in Al-Cu-Mn-Mg-Fe alloy, which can significantly refine $\text{Al}_6(\text{Mn}, \text{Fe})$ precipitates. Therefore, the mechanical properties and corrosion resistance of the alloy can be effectively improved. The study of Wang et al. [13] showed that adding Zr and Sc into Al-5Ce alloy could decrease the grain size. Compared with Zr, the yield strength can be significantly improved by adding Sc.

In order to balance the mechanical properties and thermal conductivity of Al-Cu alloys, La and Sc were added to Al-4.8Cu alloy to study the effect on microstructure, mechanical properties and thermal conductivity. The first-principles are used to calculate elastic modulus and vibrational heat capacity of some intermetallic compounds in alloys to explain the reasons for changes in the properties. Thus it can provide a theoretical basis for development of new types of high thermal conductivity aluminum alloys.

2. Materials and Methods

In this study, Al ingot with 99.9% purity, as well as commercial master alloy Al-50%Cu, Al-20%La and Al-2%Sc (all percentages are in weight unless otherwise stated) were used for casting. Firstly, pure Al and Al-50%Cu were melted at 730 °C in a resistance furnace. After completely melted, the pre-heated Al-20%La or Al-20%La+Al-2%Sc were added to the furnace. In order to ensure the uniform chemical composition of the alloy, molten metal was held for 30 min and stirred at the 20th minute. Then, we adjusted the melt temperature to 720 °C and added C_2Cl_6 with a mass of 1% of the melt mass for refining. After slag skimming, the molten metal was poured into a 250 °C metal mold ($\Phi 18 \times 150$ mm) at 700 °C. Table 1 shows the chemical composition of alloys.

Table 1. Chemical composition of the present Al-Cu, Al-Cu-La, Al-Cu-La-Sc (wt.%).

Alloy	Cu	La	Sc	Al
Al-4.8Cu	4.72	-	-	Bal.
Al-4.8Cu-0.4La	4.85	0.38	-	Bal.
Al-4.8Cu-0.4La-0.4Sc	4.78	0.37	0.42	Bal.

The specimens were polished according to the standard procedures and etched by Keller reagent. MFE-4 optical microscope (OM, NIKON instruments, (Shanghai), Co. Ltd., Shanghai, China) and FEG450 scanning electron microscope (SEM, NEC Electronics Corporation, Tokyo, Japan) were used to characterize the microstructure. In order to reduce the error, 50 grains per specimen were selected to measure the grain size by Image-Pro plus 6.0 (Sino-Vision Technology Co. Ltd., Beijing, China). D/MAX-2400 X-ray diffractometer (XRD, Rigaku, Tokyo, Japan) (2θ : 10~90°) was used to identify the specific phases in alloys. Tensile tests were carried out using a WDW-100D universal material testing machine (Jinan Hengxu Testing Machine Technology Co., Ltd., Jinan, Shandong, China) at a speed of 1 mm/min. Tests for each component of specimens were carried out three times to reduce the error. The size of the tensile specimen was designed in accordance with ASTM E8M-200 standard. MDI Jade software (5.0, CA, USA) was used to calculate the lattice constant of α -Al matrix.

LFA457 laser thermal conductivity analyzer (NETZSCH Group, Selb, Germany), STA449C (NETZSCH Group, Selb, Germany) differential scanning calorimetry tester and Archimedes drainage method were used to measure the thermal diffusivity α , specific heat capacity C_p , and density ρ , respectively. Three points of each sample were selected for testing. Then thermal conductivity can be expressed as:

$$\lambda = \alpha \rho c p \quad (1)$$

3. Results

3.1. As-Cast Microstructure Evolution

Representative optical microscope photos of as-cast microstructure are shown in Figure 1. It can be obviously seen from Figure 1a that grains of Al-Cu alloy are in the shape of dendrite and the secondary dendrite arms are extremely developed. The average grain size of α -Al is 188.89 μm . After adding La to Al-Cu alloy, as shown in Figure 1b, the morphology of grains changes from dendrite to equiaxed crystal. The secondary dendrite arms of grains almost disappear and shape distribution is relatively uniform. Simultaneously, the average grain size of α -Al decreased to 118.53 μm , which is 37.78% lower than Al-Cu. When Sc is further added to Al-Cu-La alloy, according to Figure 1c, the morphology of most grains is still in the shape of equiaxed, but a few is between equiaxed and dendrite. The average grain size of α -Al reduced to 69.25 μm , 41.6% lower than Al-Cu-La.

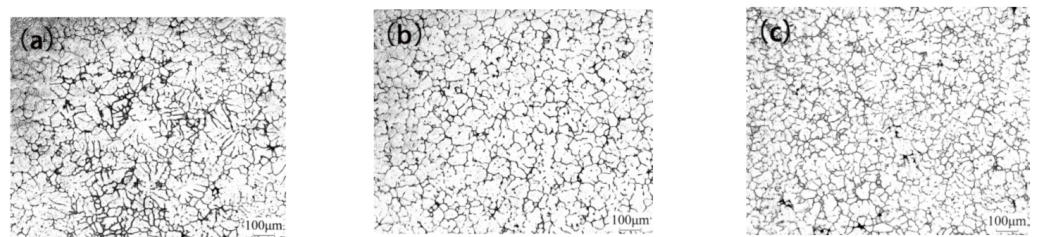


Figure 1. Representative OM images of the as-cast (a) Al-Cu, (b) Al-Cu-La, (c) Al-Cu-La-Sc alloys.

Since the atomic radius of La (0.187 nm) is 31% larger than Al (0.143 nm), it will inevitably cause great lattice distortion when La atoms enter the α -Al matrix, which will greatly increase the energy of the entire system. Therefore, the solid solubility of La atoms in the α -Al matrix is small. For the solidification process of Al-Cu-La alloy, α -Al first begins to solidify, and then low-melting-point eutectic structure containing La and Cu segregates at the grain boundary at the end of solidification [14], as shown in Figure 2. This makes the equilibrium temperature of some structures decrease. Moreover, the actual undercooling degree and the component undercooling degree at the front of the solid-liquid interface increase. So that, the grain growth is hindered and the length of the secondary dendrite arm is reduced. For Al-Cu-La-Sc alloy, an investigation presented that a ternary phase named the W-phase containing Al, Cu, and Sc, could be in thermodynamic equilibrium with α -Al at 572 $^{\circ}\text{C}$ and 546 $^{\circ}\text{C}$. Therefore, part of Sc will also exist in the low-melting-point phase at the end of solidification (Figure 3) [15].

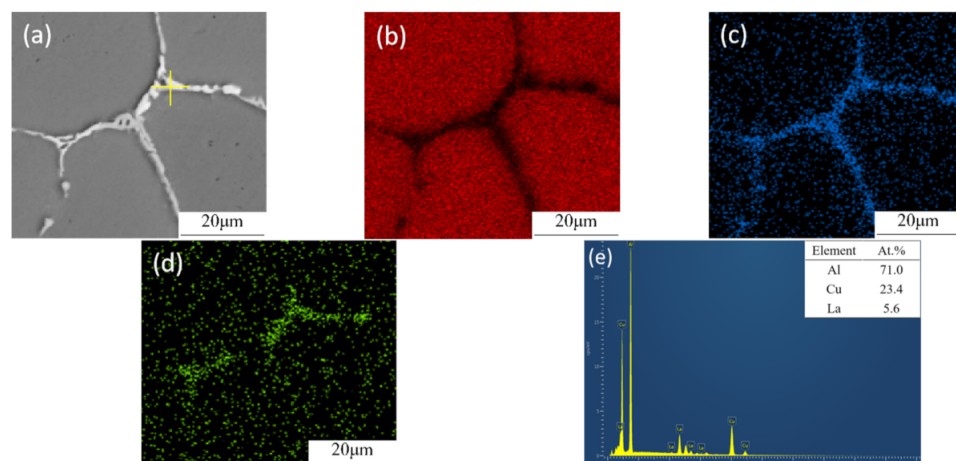


Figure 2. Map and point analysis of Al-Cu-La alloy (a) Backscattered electron image, (b) Image of Al, (c) Image of Cu, (d) Image of La, (e) Point analysis.

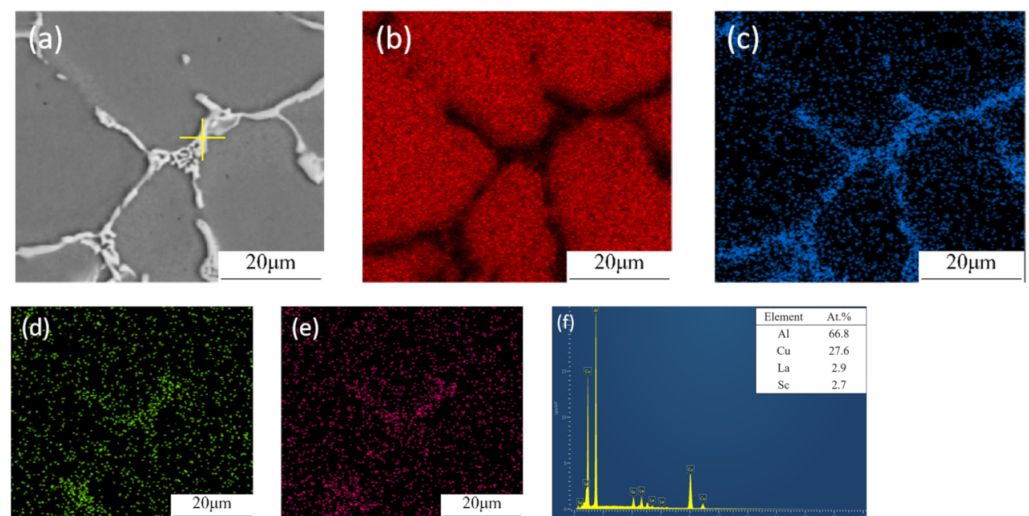


Figure 3. Map and point analysis of Al-Cu-La-Sc alloy (a) Backscattered electron image, (b) Image of Al, (c) Image of Cu, (d) Image of La, (e) Image of Sc, (f) Point analysis.

In addition, many studies have shown that Al_3Sc phase will be formed in the Al alloys with Sc [16], it nucleates before the solidification of the $\alpha\text{-Al}$ matrix [17], both of which are face-centred cubic, and the lattice constants of the $\alpha\text{-Al}$ and Al_3Sc phases are 4.089 nm and 4.049 nm, respectively. According to the disregistry equation modified by Bramfitt [18]:

$$\delta_{(hkl)_n}^{(hkl)_s} = \sum_{i=1}^3 \left[\frac{d_{[uvw]_s}^i \cos \theta - d_{[uvw]_n}^i}{d_{[uvw]_n}^i} \right] \times \frac{1}{3} \times 100\% \quad (2)$$

$(hkl)_s$ and $(kl)_n$ are the low-index plane of substrate and nucleated solid respectively, $[uvw]_s$ and $[uvw]_n$ are the low-index direction in $(hkl)_s$ and $(kl)_n$ respectively, $d_{[uvw]_s}$ and $d_{[uvw]_n}$ are the interatomic spacing along $[uvw]_s$ and $[uvw]_n$ respectively, θ is the angle between $[uvw]_s$ and $[uvw]_n$. The above formula can calculate the disregistry between Al_3Sc and $\alpha\text{-Al}$ as 0.99%. Studies have shown that when the disregistry is less than 5%, the elastic energy caused by direct connection of atoms on both sides of the phase interface is small, and the interface can be considered as completely coherent. And Al_3Sc can be used as a heterogeneous nucleation center to refine the $\alpha\text{-Al}$ matrix. Due to the same cooling condition the alloys have, the $\alpha\text{-Al}$ in Al-Cu-La-Sc alloy will nucleate at a higher temperature and have more time to grow. This leads to more developed dendrite arms than Al-Cu-La before the solidification of the low melting point phase. Therefore, Figure 1 shows that the number of dendrite grains in Al-Cu-La-Sc alloy has a slight increase compared with Al-Cu-La.

3.2. Mechanical Properties

The mechanical properties and engineering stress-strain curves of alloys are presented in Figure 4. It can be seen that the tensile strength and yield strength of Al-Cu-La and Al-Cu-La-Sc are significantly improved compared with Al-Cu. Al-Cu-La-Sc has the highest tensile strength and yield strength of 227.6 ± 5.0 MPa and 157.3 ± 3.6 MPa, which are 55.1% and 65.2% higher than the 146.7 ± 7.5 MPa and 95.2 ± 5.3 MPa of Al-Cu. The tensile strength and yield strength of Al-Cu-La are 175.2 ± 4.4 MPa and 112.4 ± 2.1 MPa, respectively, which are 19.4% and 18.1% higher than Al-Cu. The elongation of Al-Cu-La and Al-Cu-La-Sc are $10.35\% \pm 0.30\%$ and $9.17\% \pm 0.38\%$, which are 34.4% and 19.1% higher than the $7.70\% \pm 0.50\%$ of Al-Cu, respectively.

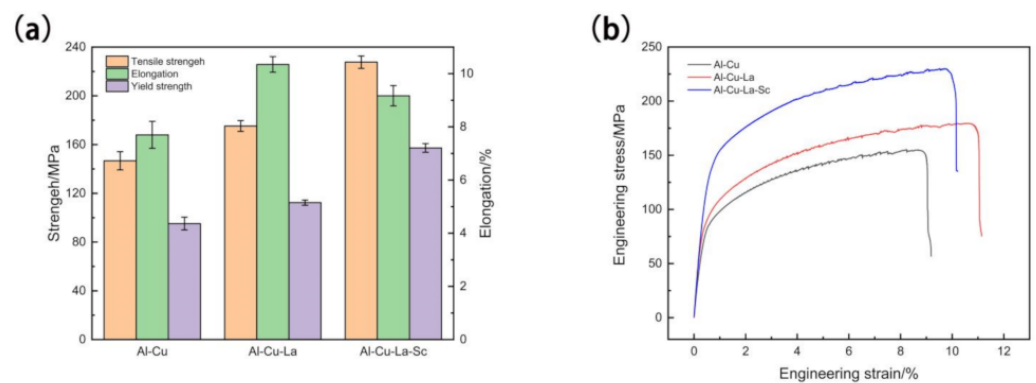


Figure 4. The mechanical properties (a) and engineering stress-strain curves (b) of Al-Cu, Al-Cu-La, Al-Cu-La-Sc alloys.

The addition of La and Sc can reduce the grain size and make the shape distribution uniform of Al-Cu alloy. Many studies have proved that the yield strength and grain size of metal materials conform to the Hall-Petch equation [19]:

$$\sigma_s = \sigma_0 + k_d d^{-\frac{1}{2}} \quad (3)$$

where σ_s is the yield stress of specimen, σ_0 is a constant related to the starting stress for dislocation movement, k is the coefficient of strengthening, d is the average diameter of grain. According to the equation above, the smaller the grain size, the higher the yield strength of the material, which is consistent with the aforementioned experimental results.

3.3. Properties of Thermal Conductivity

Figure 5 shows the thermal conductivity, specific heat capacity and thermal diffusivity of alloys. As shown in Figure 5a, when La and La+Sc were added to Al-Cu, the thermal conductivity of alloys are $206.286 \text{ W}\cdot\text{m}^{-1}\cdot\text{K}^{-1}$ and $199.667 \text{ W}\cdot\text{m}^{-1}\cdot\text{K}^{-1}$, respectively, which are 10.0% and 6.5% higher than $187.489 \text{ W}\cdot\text{m}^{-1}\cdot\text{K}^{-1}$ of Al-Cu. It can be seen from Figure 5b that the specific heat capacity of Al-Cu-La decreases from $0.972 \text{ J}\cdot\text{g}^{-1}\cdot\text{K}^{-1}$ to $0.941 \text{ J}\cdot\text{g}^{-1}\cdot\text{K}^{-1}$ compared with Al-Cu, and the thermal diffusivity increases from $72.76 \text{ mm}^2\cdot\text{s}^{-1}$ to $79.14 \text{ mm}^2\cdot\text{s}^{-1}$. Compared with Al-Cu-La, the specific heat capacity of Al-Cu-La-Sc increases to $0.965 \text{ J}\cdot\text{g}^{-1}\cdot\text{K}^{-1}$ and thermal diffusivity decreases to $74.53 \text{ mm}^2\cdot\text{s}^{-1}$.

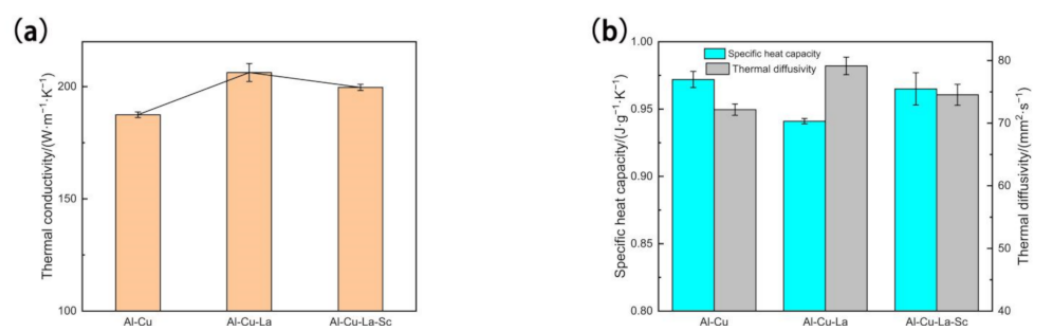


Figure 5. Properties of thermal conductivity of Al-Cu, Al-Cu-La, Al-Cu-La-Sc alloys: (a) Thermal conductivity, (b) Specific heat capacity and Thermal diffusivity.

3.4. Fracture Morphology

Figure 6a–f shows the fracture morphology of alloys. Figure 6d–f are the enlarged images in the yellow square of Figure 6a–c. There are a few dimples in the upper right part of Figure 6a,d and the lower left part is similar to the pattern of shear fracture. This is caused by pores in the alloy, resulting in the fracture surface not perpendicular to the

stress direction, as shown in Figure 6g. Figure 6b,e present that there are many dimples in the fracture surface of Al-Cu-La alloy. It can be concluded that the fracture mode is ductile failure, the addition of La did not change the fracture mode of Al-Cu alloy. Furthermore, the number of dimples in Al-Cu-La alloy is more than Al-Cu, and the shape is more uniform. Therefore, the plasticity and toughness of Al-Cu-La alloy are better than Al-Cu. The fracture mode of the Al-Cu-La-Sc alloy is obviously different from the former two, as shown in Figure 6c,f. It is transgranular failure with a small number of dimples and tearing ridges. Cleavage steps and river patterns can also be seen in the surface. So the fracture mode of Al-Cu-La-Sc can be concluded as quasi-cleavage fracture transition from ductile to brittle. As a consequence, the yield strength of Al-Cu-La-Sc alloy is higher than the two without Sc addition, but the elongation is lower than Al-Cu-La alloy.

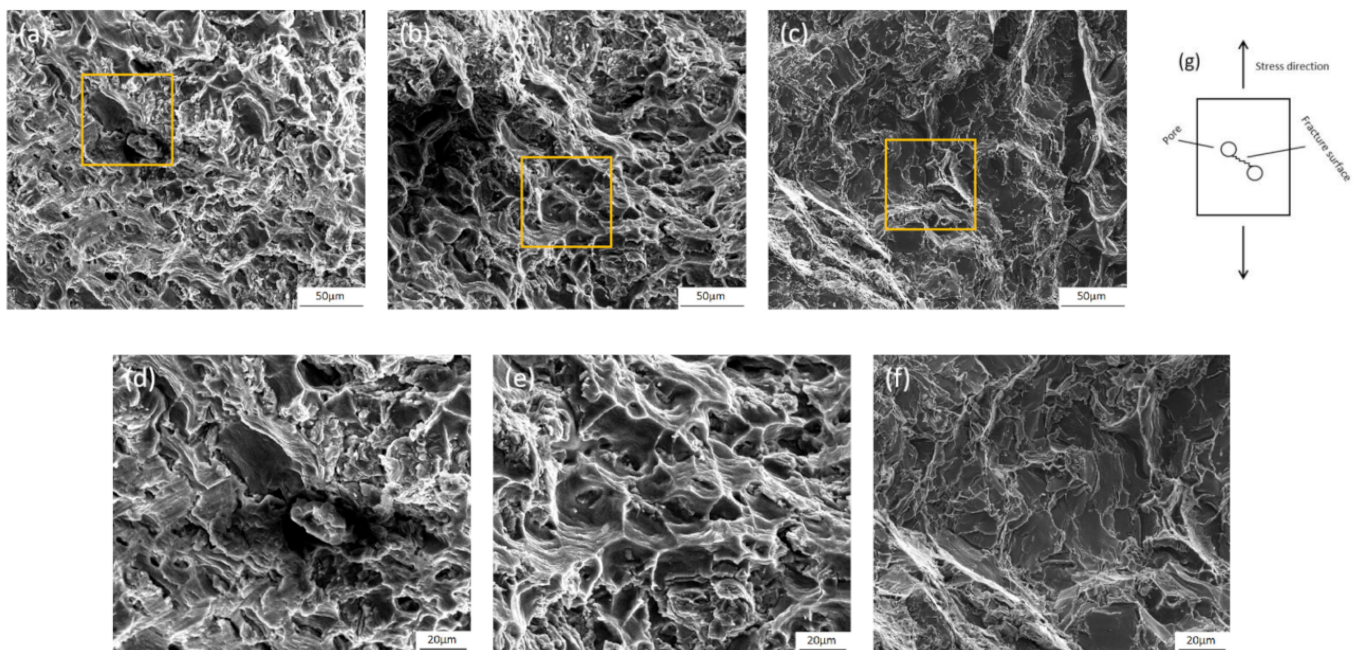


Figure 6. Fracture morphology of (a), (d) Al-Cu; (b), (e) Al-Cu-La; (c), (f) Al-Cu-La-Sc alloys. (g) Effect of pores on fracture morphology.

3.5. Lattice Distortion

The lattice constants of the α -Al matrix in pure Al, Al-Cu, Al-Cu-La, Al-Cu-La-Sc alloys are shown in Figure 7. Since the atomic radius of Cu is 0.128 nm which is smaller than Al, and the maximum solubility of Cu in Al is 5.65% at 548.2 °C, the supersaturated substitutional solid solution will be formed during the cooling process. As a result, the lattice constant of Al-Cu alloy is less than pure Al. Due to the α -Al precipitates before the La-containing phase during the solidification process, and it is difficult for La atoms to enter the α -Al matrix, the lattice constant of Al-Cu is slightly higher than Al-Cu-La. For Al-Cu-La-Sc alloy, the Al_3Sc phase will precipitate above 660 °C during solidification, which makes Al matrix heterogeneous nucleation and growth near its equilibrium solidification temperature. Therefore, the solid solubility of Cu and La elements in the α -Al matrix is reduced, and the lattice constant of the Al-Cu-La-Sc alloy is close to pure Al. Table 2 shows the spacing between atomic layers (d-spacing) of different crystal plane set. It can be seen that the variation of d-spacing is consistent with the lattice constants.

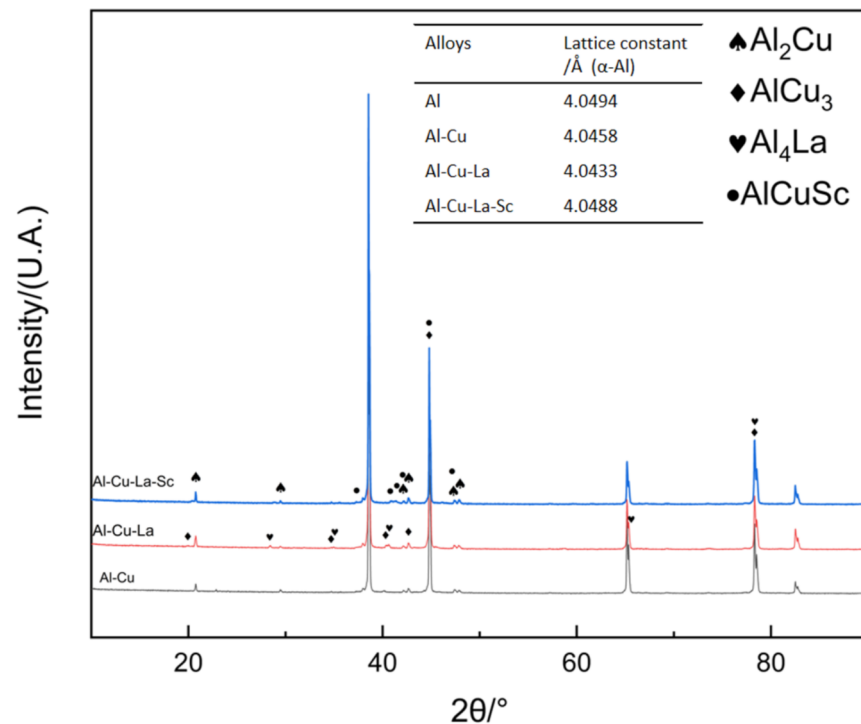


Figure 7. XRD patterns and α -Al lattice constants of Al-Cu, Al-Cu-La, Al-Cu-La-Sc alloys.

Table 2. The d-spacing and diffraction angle of different crystal plane set in Al-Cu, Al-Cu-La, Al-Cu-La-Sc alloys.

Crystal Plane Set	Al-Cu		Al-Cu-La		Al-Cu-La-Sc	
	$2\theta/(\circ)$	d-Spacing/Å	$2\theta/(\circ)$	d-Spacing/Å	$2\theta/(\circ)$	d-Spacing/Å
{111}	38.509	2.3359	38.534	2.3344	38.479	2.3376
{200}	44.763	2.0229	44.793	2.0216	44.729	2.0244
{220}	65.163	1.4304	65.209	1.4295	65.109	1.4315
{311}	78.313	1.2199	78.372	1.2191	78.245	1.2208
{222}	82.527	1.1679	82.590	1.1672	82.453	1.1688

Also, it can be inferred that the variation tendency of Cu percentage at the grain boundary decreases first and then increases. Researchs have shown that for the intermetallic compounds containing Al and Cu, the higher the content of Cu, the greater the brittleness [20,21]. This is consistent with the above experimental results.

3.6. Intermetallic Compounds at Grain Boundaries

According to the Map scanning results of Figure 2, it can be seen that the low-melting-point phase at the grain boundary of Al-Cu-La alloy is composed of Al, Cu, and La. The atomic proportion of Al and Cu in the point scan result in Figure 2e is removed according to 2:1, the remaining Al:La is about 4.3:1. Combined with the XRD results in Figure 7, it can be concluded that the La-containing phase in Al-Cu-La alloy is Al₄La [22]. In the same way, it can be calculated that the Sc-containing phase formed at the end of solidification at the grain boundary of Al-Cu-La-Sc alloy is AlCuSc, combining Figures 3f and 7.

4. Discussion

4.1. Grain Refinement of Alloys with La and La + Sc Addition

JMatPro software was used to calculate the specific heat capacity of Al-Cu, Al-Cu-La, Al-Cu-La-Sc alloys at different temperatures in the equilibrium solidification state, as shown in Figure 8. According to the Al-Cu phase diagram, the initial solidification temperature of Al-4.8Cu alloy is about 647 °C. The solidification of α -Al at this temperature will release a large amount of latent heat of crystallization, which causes the specific heat capacity of alloys to undergo abrupt changes. As can be seen from Figure 8, the existence of the low melting point eutectic leads to a sudden change in the specific heat capacity of alloys at 546 °C. Figure 8a shows that the specific heat capacity of Al-Cu alloy is $31.48 \text{ J}\cdot\text{g}^{-1}\cdot\text{K}^{-1}$ at about 647 °C, and $29.32 \text{ J}\cdot\text{g}^{-1}\cdot\text{K}^{-1}$ at about 546 °C. For Al-Cu-La alloy (Figure 8b), the specific heat capacity is $28.39 \text{ J}\cdot\text{g}^{-1}\cdot\text{K}^{-1}$ at about 647 °C, and $29.11 \text{ J}\cdot\text{g}^{-1}\cdot\text{K}^{-1}$ at about 546 °C, which is higher than the former. And the specific heat capacity at 585 °C increased slightly from $1.942 \text{ J}\cdot\text{g}^{-1}\cdot\text{K}^{-1}$ to $2.786 \text{ J}\cdot\text{g}^{-1}\cdot\text{K}^{-1}$ due to the existence of La-containing phase [14]. It can be concluded that after adding La to Al-Cu alloy, the latent heat of crystallization released during solidification of low-melting-point phase with a great degree of undercooling in the later stage of solidification will cause necking and remelting at the junction of secondary dendrite arm and dendrite trunk with large surface energy. Finally, the number of grains increases and the grain size decreases. For Al-Cu-La-Sc alloy, the specific heat capacity increases sharply to $56.96 \text{ J}\cdot\text{g}^{-1}\cdot\text{K}^{-1}$ at about 546 °C, however, it is $28.64 \text{ J}\cdot\text{g}^{-1}\cdot\text{K}^{-1}$ at 647 °C, which is almost unchanged. Therefore, the latent heat of crystallization released when the low-melting-point phase solidifies has a more obvious effect on the fusing and breaking of secondary dendrite arms.

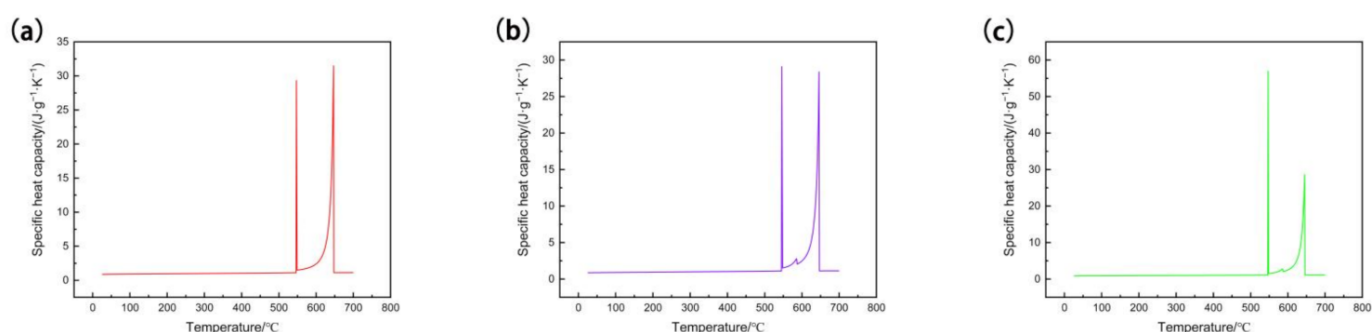


Figure 8. Variation trend of specific heat capacity of (a) Al-Cu, (b) Al-Cu-La, (c) Al-Cu-La-Sc alloys with temperature in equilibrium solidification state.

4.2. Effect of La and La + Sc on the Porosity

Figure 9 shows the ratio of measured density to the ideal density of alloys at 25 °C calculated by JMatPro software. The ratios of Al-Cu, Al-Cu-La, and Al-Cu-La-Sc increase sequentially, indicating that the volume fraction of shrinkage porosity decreases in order. Figure 10 shows the DSC curves of alloys, the ratio of endothermic peak height cannot be used as the ratio of specific heat capacity of the corresponding phase due to the specimen weight used in the DSC test is less than 0.05 g, the distribution of each phase in such a small volume is not uniform. However, the initial melting and complete melting temperatures of alloys are not affected. Figure 10 presents that the solidification temperature range of Al-Cu alloy is about 108 °C, that is to say, the solidification mode tends to be pasty solidification. During the cooling process, the α -Al matrix grows in the shape of dendrite, and the specific surface area of grains is large, it can be seen from Figure 1a that the roundness of grains is poor. The closed spaces generated by the overlapping of dendrite arms is easy to appear, so that the low-melting-point phase at the end of solidification can not fill these pores, and has a great tendency of hot tearing [23], as shown in Figure 11a. Furthermore, the Al-Cu alloy has a huge linear shrinkage coefficient. If there is no filling of low-melting-point

phase between two originally contacting grains, the intergranular separation stress will also generate pores between grains during the cooling process. In addition, the gas sucked into the melt during alloy smelting will precipitate out in the form of pores during the cooling process. Due to the existence of pores, the actual area of thrust surface of the alloy during the tensile test is smaller than the cross-sectional area of tensile specimen. The cracks will first occur and spread near the pore when the tensile specimen starts to fracture. That will do great harm to the mechanical properties of alloys.

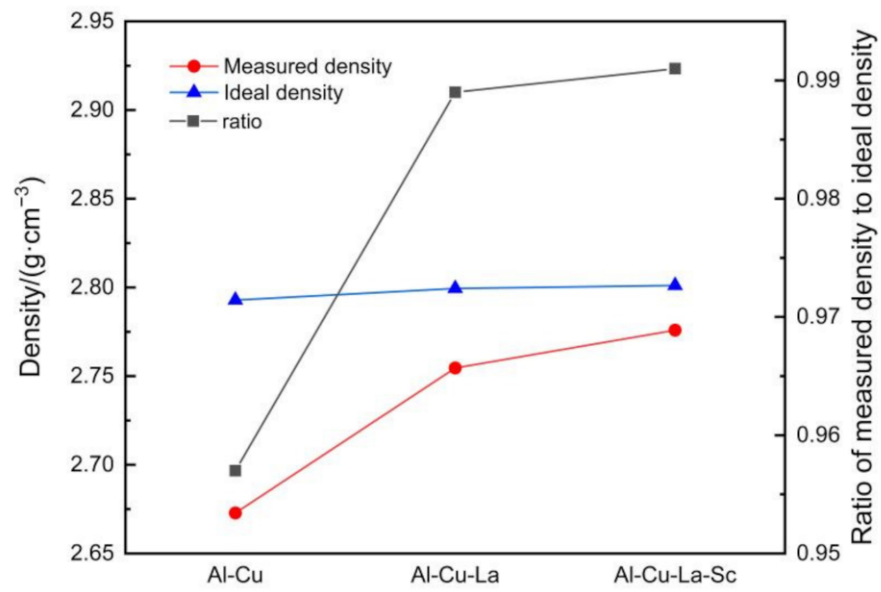


Figure 9. The ratio of measured density to ideal density of Al-Cu, Al-Cu-La, Al-Cu-La-Sc alloys.

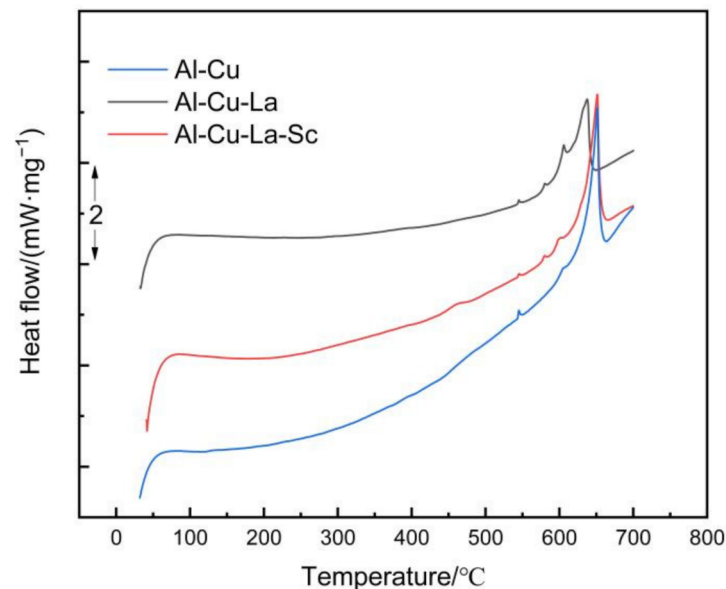


Figure 10. DSC curves of Al-Cu, Al-Cu-La, Al-Cu-La-Sc alloys.

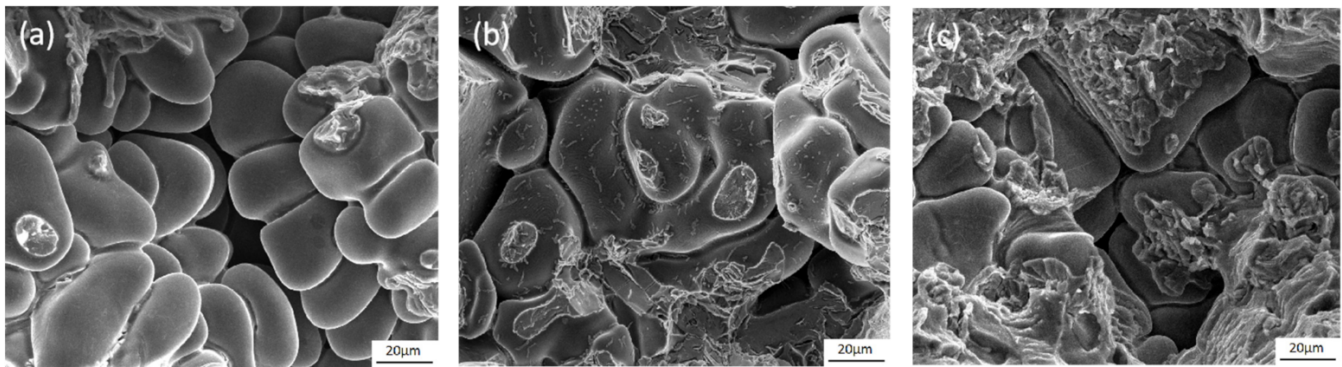


Figure 11. Intergranular morphology of (a) Al-Cu, (b) Al-Cu-La, (c) Al-Cu-La-Sc alloys.

After adding La to Al-Cu alloy, it will first form a stable hydride LaH_2 with H element entering the melt, which will be discharged out of the melt during the slagging process. Figure 10 shows that the solidification temperature range of Al-Cu-La is 92°C , which is 16°C lower than Al-Cu alloy. On one hand, the shortening of solidification temperature range leads to the increase of alloy fluidity at the same temperature, and solidification mode is excessive from pasty solidification to sequential solidification, this also improves the feeding capacity of the metal melt. On the other hand, part of the secondary dendrite arms are fused at the end of solidification, the feeding channel is opened. The low-melting-point phase forms a liquid film among grains when the bonding force of the liquid film is greater than intergranular separation stress, the liquid film will be stretched rather than broken, as shown in Figure 11b. The solidification temperature range of Al-Cu-La-Sc alloy is not much different from Al-Cu due to the heterogeneous nucleation caused by Al_3Sc particles. However, the filling ability of Al-Cu-La-Sc alloy is slightly improved and the porosity is further reduced [24]. This is because the grain size of Al-Cu-La-Sc is significantly lower than Al-Cu. For the above reasons, the mechanical properties of Al-Cu-La and Al-Cu-La-Sc alloys are improved compared with that of Al-Cu.

4.3. Effect of Structure Change on Electron Transport

For alloys, the carriers of heat transfer include electrons and lattice waves generated by lattice vibrations (phonon), and electron heat conduction plays a major role. According to the free electron theory, the free electrons travel in crystal lattice according to the law of wave mechanics. The mean free path of electrons is equivalent to the size of the crystal when the crystal lattice is intact, and its propagation will not be hindered. Nevertheless, according to Matthiessen's law [25], there will be impurities and defects in the alloy under normal conditions. The dynamic lattice distortion caused by thermal vibration of impurities and static lattice distortion caused by defects will scatter the electron waves, which will result in the decrease of the electrical conductivity of the alloy. Widemann-Franz [26] law indicates that the ratio of thermal conductivity and electrical conductivity of some metals has a linear relationship with temperature. When the temperature is constant, the ratio is a fixed value. Therefore, the factors causing the increase of alloy thermal resistance can be expressed as:

$$\rho = \rho_T + \rho_r \quad (4)$$

$$\rho_r = \rho_{md} + \rho_p \quad (5)$$

ρ is the total thermal resistance of the metallic materials; ρ_T is the thermal resistance related to temperature; ρ_r is the residual thermal resistance related to defects. ρ_r can be expressed as the sum of ρ_{md} and ρ_p . ρ_{md} is the thermal resistance caused by micro defects such as grain boundary, dislocation, solid solution atom and second phase precipitation; ρ_p is the macroscopic casting defects such as shrinkage cavity and porosity and crack.

According to the above experimental results, Al-Cu alloy has the highest proportion of pores, which strongly hinder and scatter the transfer of free electrons during heat

conduction. Furthermore, heat conduction can only be carried out through radiation at the vacuum layer generated by intergranular separation stress. These result in low thermal diffusivity of the alloy [27]. After adding La to Al-Cu alloy, the porosity of the alloy decreases and the proportion of grain boundary increases. The thermal conductivity of air in the enclosed environment is about $0.023 \text{ W}\cdot\text{m}^{-1}\cdot\text{K}^{-1}$, while the Al_2Cu phase at room temperature is between $120\text{--}130 \text{ W}\cdot\text{m}^{-1}\cdot\text{K}^{-1}$ [28]. Therefore, the decrease in electron scattering caused by the decrease of porosity is greater than the increase in the effect of the increase of grain boundaries on electron scattering. Compared with Al-Cu-La alloy, the porosity of Al-Cu-La-Sc is not significantly reduced, but the grain size is greatly reduced. At this time, the increase in the proportion of grain boundaries will greatly increase the scattering effect of electron transfer. In addition, studies have shown that the larger the spacing of the atomic layers, the smaller the obstacle to electron transfer [29]. However, it can be seen from Figure 5a and Table 2 that in the as-cast Al-Cu alloy without additional pressure treatment, the effect of pores and grain boundaries on electron transfer is greater than the spacing of the atomic layers.

4.4. First-Principles Study of Intermetallic Compounds in Al-Cu, Al-Cu-La, Al-Cu-La-Sc Alloys

All the calculation was carried out by the Castep module based on density functional theory (DFT) of Materials Studio software. The choice of exchange-correlation energy functional is the PEB (Perdew Burke Ernzerhof) form in the GGA (Generalized Gradient Approximation) [30]. Ultrasoft [31] was used to study the Coulomb attraction between multiple particles. Cell shape and cell volume using a convergent energy cut-off of 450 eV for AlCuSc with $12 \times 12 \times 10$ k-point, and 380 eV for Al_2Cu , AlCu_3 , Al_4La , Al_3Sc with $8 \times 8 \times 8$ k-point. The lattice constants data of intermetallic compounds is shown in Table 3, and the crystal structure model is shown in Figure 12.

Table 3. Calculated lattice constants data of intermetallic compounds.

Phase	Space Group	Crystal System	$a(\text{\AA})$	$b(\text{\AA})$	$c(\text{\AA})$
Al_2Cu	I4/mcm	Tetragonal	6.0379	6.0379	4.9351
AlCu_3	Fm-3m	Cubic		5.8369	
Al_4La	I4/mmm	Tetragonal	4.3558	4.3558	10.2396
Al_3Sc	Pm-3m	Cubic		4.1173	
AlCuSc	Amm2	Orthorhombic	5.2007	5.2007	8.3881

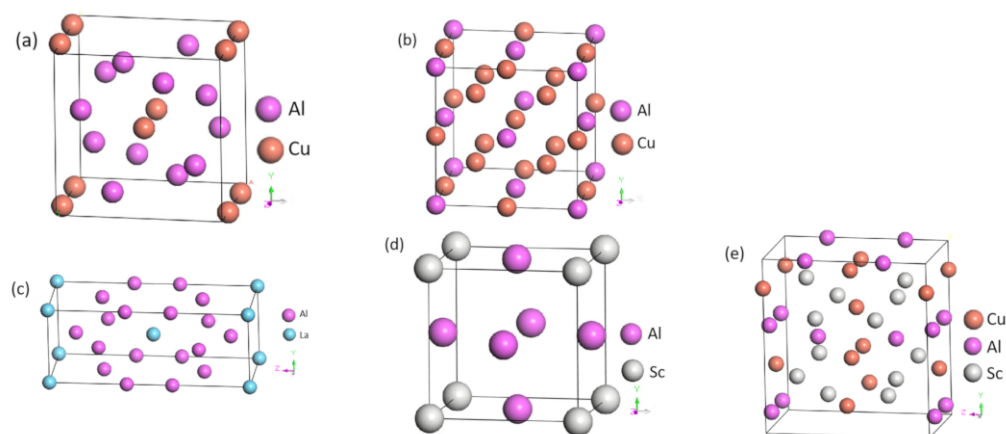


Figure 12. Crystal structure model of intermetallic compounds. (a) Al_2Cu , (b) AlCu_3 , (c) Al_4La , (d) Al_3Sc , (e) AlCuSc .

4.4.1. First-Principles Calculations for Mechanical Properties

The elastic constant of intermetallic compounds was obtained by calculation, using the Voigt-Reuss-Hill (VRH) approximation method to obtain bulk modulus (B), shear modulus

(G), Young's modulus (E) [32,33]. In addition, the B/G value and Poisson's ratio (ν) can also be calculated for all phases [34], as shown in Table 4. The value of B/G can be used as an empirical criterion to judge the ductility of materials [35], ductility and toughness increase with the increase of B/G value. Generally, the critical value of brittleness and toughness is taken as 1.75. Poisson's ratio can also be used as a basis judgement for brittleness and toughness of materials. It is usually considered that the material has better plasticity and toughness when Poisson's ratio is greater than 0.26. Young's modulus expresses the ability of materials to resist stress and strain in the process of elastic deformation. The greater the Young's modulus, the greater the stiffness.

Table 4. Bulk modulus B (GPa), shear modulus G (GPa), Young's modulus E (GPa), G/B and Poisson's ratio ν of intermetallic compounds.

Phase	B	G	E	B/G	ν
Al_2Cu	98.48	44.88	116.87	2.19	0.30
AlCu_3	135.69	43.75	118.52	3.10	0.35
Al_4La	69.59	24.62	66.07	2.83	0.34
Al_3Sc	84.20	71.25	166.72	1.18	0.17
AlCuSc	123.99	60.69	156.52	2.04	0.28

According to foregoing conclusions, Al_4La phase was formed at the grain boundaries after adding La to Al-Cu alloy, and Figure 7 shows that AlCu_3 phase appears in Al-Cu-La alloy. The B/G value and Poisson's ratio of Al_4La and AlCu_3 are both larger than Al_2Cu . Young's modulus of Al_4La is much smaller than Al_2Cu . These lead to an increase in the elongation of Al-Cu-La alloy. The number and depth of dimples at the fracture also increased (Figure 6). Therefore, Al-Cu-La alloy shows excellent ductility and toughness.

As Figure 7 presents, the AlCu_3 is reduced after adding Sc to the Al-Cu-La alloy. The B/G value of Al_3Sc that precipitated first during the solidification process is less than 1.75, and Poisson's ratio of Al_3Sc is 0.17. The B/G value and Poisson ratio of AlCuSc that formed at the end of solidification are both smaller than AlCu_3 and Al_4La . Young's modulus of Al_3Sc and AlCuSc are much higher than other phases. These factors show that the barrier of grain boundary to grain deformation is more obvious. So the elastic deformation of Al-Cu-La-Sc under the same force is small. It has poor ductility and toughness, and the elongation is lower than that of Al-Cu-La. Moreover, the surface of fracture presents a brittle fracture morphology.

4.4.2. First-Principles Calculations for Vibrational Heat Capacity

The ratio of the contribution of free electron gas and lattice vibration to molar heat capacity is:

$$\frac{c_V^e}{c_V^a} = \frac{5Z\theta_D^3}{24\pi^2 T_F} \cdot \frac{1}{T^2} \quad (6)$$

Z is the number of valence electrons per atom; θ_D is the Debye temperature; T_F is the Fermi temperature; T is the actual temperature. It can be observed that the value of the above equation decreases with the increase of actual temperature. When the temperature is lower than 10 K, the vibrational heat capacity will be less than the electron heat capacity. At ambient temperature, the contribution of the free electron to heat capacity can be neglected. Hence, only the vibrational heat capacity is considered in this paper.

This paper uses the Al_3Cu phase with a lattice structure of pm-3m which replaces the two opposite face-centered Al atoms with Cu atoms to approximate the influence of Cu atoms in solid solution state on the vibrational heat capacity.

Materials studio software CASTEP module was used to calculate the phonon scattering and density of states, then obtain the vibrational heat capacity of each phase at a temperature of 0–1000 K through analysis, as shown in Figure 13. The dotted line is the vibrational heat capacity of different phases at 298.15 K. After adding La to Al-Cu alloy, the

lattice constant does not change significantly, which indicates that the solid solubility of Cu in Al has no obvious change. The appearance of Al_4La and AlCu_3 phases indicates that the content of the Al_2Cu phase decreases. The vibrational heat capacity of Al_4La and AlCu_3 phases is smaller than Al_2Cu and Al. On the other hand, the porosity of Al-Cu-La alloy is reduced, and the specific heat capacities of H_2 and N_2 are much higher than Al. In summary, the specific heat capacity of Al-Cu-La alloy is slightly smaller than Al-Cu. Compared with Al-Cu-La, Al-Cu-La-Sc alloy has a smaller lattice distortion, which demonstrates that the content of Cu atoms in the Al matrix is reduced. Figure 13 shows that the vibrational heat capacity of Al_3Cu is smaller than pure Al and Al_2Cu phase. AlCuSc has the highest vibrational heat capacity in all phases, and the vibrational heat capacity of Al_3Sc is only smaller than AlCuSc and Al_2Cu . As a result, the specific heat capacity of Al-Cu-La-Sc is slightly higher than Al-Cu-La.

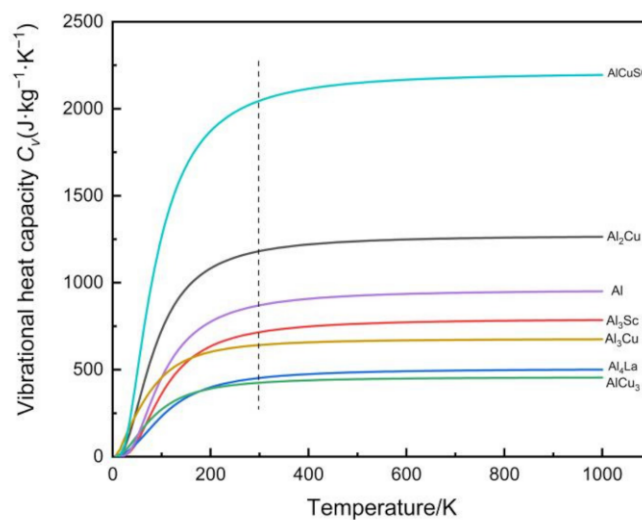


Figure 13. Vibrational heat capacity of different phases at 0–1000 K.

4.4.3. Discussion on Thermal Diffusivity

Thermal diffusivity is a physical quantity that characterizes the increase in temperature of an object. For alloys, it is related to the specific heat capacity and electron transfer. Since the vibrational heat capacity of Al-Cu-La is smaller than Al-Cu and Al-Cu-La-Sc, the temperature rise of Al-Cu-La will be higher than the other two when transferred energy is the same. In addition, the reduction of porosity compared with Al-Cu and the reduction of the proportion of grain boundaries compared with Al-Cu-La-Sc enable Al-Cu-La to transfer more energy than the other two at uniform conditions. As a consequence, the thermal diffusivity of Al-Cu-La is greater than Al-Cu and Al-Cu-La-Sc.

From the discussion above, if the intermetallic compounds that may exist in the alloy are known in advance, the properties of intermetallic compounds can be calculated by first-principles calculation. Thus, the possible changes in the properties of the alloy can be inferred without specific tests. This can greatly reduce the experimental cost and provide new possibilities for the development of aluminum alloys.

5. Conclusions

1. Adding La and La+Sc to Al-Cu alloy can significantly refine the α -Al matrix. The grain morphology changes from coarse dendrite to fine equiaxed crystal. The grain sizes of Al-Cu-La and Al-Cu-La-Sc alloys are $118.53 \mu\text{m}$ and $69.25 \mu\text{m}$, respectively, which are 37.78% and 63.33% lower than the $188.89 \mu\text{m}$ of Al-Cu.
2. La and La+Sc can significantly improve the mechanical properties and thermal conductivity of Al-Cu alloy. Al-Cu-La has the highest elongation of $10.35\% \pm 0.30\%$, which is 34.4% higher than the $7.70\% \pm 0.50\%$ of Al-Cu. Al-Cu-La-Sc has the high-

est tensile strength and yield strength of 227.6 ± 5.0 MPa and 157.3 ± 3.6 MPa, which are 55.1% and 65.2% higher than the 146.7 ± 7.5 MPa and 95.2 ± 5.3 MPa of Al-Cu, respectively. The thermal conductivity of Al-Cu-La and Al-Cu-La-Sc are $206.286 \text{ W}\cdot\text{m}^{-1}\cdot\text{K}^{-1}$ and $199.667 \text{ W}\cdot\text{m}^{-1}\cdot\text{K}^{-1}$, respectively, which are 10.0% and 6.5% higher than $187.489 \text{ W}\cdot\text{m}^{-1}\cdot\text{K}^{-1}$ of Al-Cu.

- The properties of intermetallic compounds in alloys were calculated by first-principles calculations. Al_4La and AlCu_3 in Al-Cu-La have good ductility, but the vibrational heat capacity at 25 °C is very low. Al_3Sc and AlCuSc in Al-Cu-La-Sc are brittle phases with high resistance to deformation. However, the toughness is poor, and the vibrational heat capacity is higher than Al_4Cu and AlCu_3 . The first principle calculation provides another way for developing new alloy materials according to the performance requirements. The general change trend of alloy properties can be inferred without specific experiment.

Author Contributions: Methodology, Z.-X.S. and H.-K.Y.; software, Z.-X.S. and W.-J.L.; formal analysis, Z.-X.S. and Y.-J.C.; investigation, Z.-X.S. and Y.-J.C.; resources, Y.-D.L. and G.-L.B.; writing—original draft preparation, Z.-X.S. and W.-J.L.; writing—review and editing, Z.-X.S., W.-J.L. and H.-K.Y.; project administration, Y.-D.L. and G.-L.B.; funding acquisition, Y.-D.L. and G.-L.B. All authors have read and agreed to the published version of the manuscript.

Funding: This work is financially supported by the National Key Research and Development Program (No. 2018YFB2001800) and the National Natural Science Foundation of China (Nos. 51961021 and 52001152).

Institutional Review Board Statement: Not applicable.

Informed Consent Statement: Not applicable.

Data Availability Statement: Not applicable.

Conflicts of Interest: The authors declare no conflict of interest.

References

- Janicki, M.; Napieralski, A. Modelling electronic circuit radiation cooling using analytical thermal model. *Microelectron. J.* **2000**, *31*, 781–785. [\[CrossRef\]](#)
- Li, J.; Lv, L.; Zhou, G.H.; Li, X.P. Mechanism of a microscale flat plate heat pipe with extremely high nominal thermal conductivity for cooling high-end smartphone chips. *Energy Convers. Manag.* **2019**, *201*, 112202. [\[CrossRef\]](#)
- Dong, Z.Q.; Wang, J.G.; Guan, Z.P.; Ma, P.K.; Zhao, P.; Li, Z.J.; Liu, T.S.; Yan, R.F. Effect of Short T6 Heat Treatment on the Thermal Conductivity and Mechanical Properties of Different Casting Processes Al-Si-Mg-Cu Alloys. *Metals* **2021**, *11*, 1450. [\[CrossRef\]](#)
- Li, S.B.; Yang, X.Y.; Hou, J.T.; Du, W.B. A review on thermal conductivity of magnesium and its alloys. *J. Magnes. Alloys* **2020**, *8*, 78–90. [\[CrossRef\]](#)
- Zhang, K.; Tao, P.; Zhang, Y.H.; Liao, X.P.; Nie, S.X. Highly thermal conductivity of CNF/AlN hybrid films for thermal management of flexible energy storage devices. *Carbohydr. Polym.* **2019**, *213*, 228–235. [\[CrossRef\]](#)
- He, T.; Chen, S.; Lu, T.; Zhao, P.; Chen, W.; Scudino, S. High-strength and ductile ultrafine-grained Al-Y-Ni-Co alloy for high-temperature applications. *J. Alloys Compd.* **2020**, *848*, 156655. [\[CrossRef\]](#)
- Cheng, W.; Liu, C.Y.; Huang, H.F.; Zhang, L.; Zhang, B.; Shi, L. High strength and ductility of Al-Si-Mg alloys fabricated by deformation and heat treatment. *Mater. Charact.* **2021**, *178*, 111278. [\[CrossRef\]](#)
- Ren, P.R.; Song, W.; Zhong, G.; Huang, W.Q.; Zuo, Z.X.; Zhao, C.Z.; Yan, K.J. High-cycle fatigue failure analysis of cast Al-Si alloy engine cylinder head. *Eng. Fail. Anal.* **2021**, *127*, 105546. [\[CrossRef\]](#)
- Karabay, S. Modification of AA-6201 alloy for manufacturing of high conductivity and extra high conductivity wires with property of high tensile stress after artificial aging heat treatment for all-aluminium alloy conductors. *Mater. Des.* **2006**, *27*, 821–832. [\[CrossRef\]](#)
- Zhai, F.L.; Wang, L.P.; Gao, X.; Feng, Y.C.; Zhao, S.C.; Wang, L. Study on Phases Formation and Modification Ability of Rare Earth Elements La, Ce, Sm and Er in Al-Zn-Mg-Cu-Zr Alloy. *Trans. Indian Inst. Met.* **2021**, *74*, 2639–2649. [\[CrossRef\]](#)
- Zheng, Q.J.; Jiang, H.X.; He, J.; Zhang, L.L.; Zhao, J.Z. Effect of micro-alloying La on precipitation behavior, mechanical properties and electrical conductivity of Al-Mg-Si alloys. *Sci. China Technol. Sci.* **2021**, *64*, 2012–2022. [\[CrossRef\]](#)
- Du, J.D.; Ding, D.Y.; Zhang, W.L.; Xu, Z.; Gao, Y.J.; Chen, G.Z.; You, X.H.; Chen, R.Z.; Huang, Y.W.; Tang, J.S. Effect of Ce addition on the microstructure and properties of Al-Cu-Mn-Mg-Fe lithium battery shell alloy. *Mater. Charact.* **2018**, *142*, 252–260. [\[CrossRef\]](#)

13. Wang, L.Y.; Ye, B.; Bai, Y.; Zhao, B.B.; Ding, W.J. Effect of Zr and Sc micro-additions on the microstructure and mechanical properties of as-cast Al-5Ce alloy. *Mater. Sci. Eng. A* **2021**, *822*, 141654. [[CrossRef](#)]
14. Mahmoud, M.G.; Samuel, A.M.; Doty, H.W.; Samuel, F.H. Effect of the Addition of La and Ce on the Solidification Behavior of Al-Cu and Al-Si-Cu Cast Alloys. *Int. J. Met.* **2019**, *14*, 191–206. [[CrossRef](#)]
15. Røyset, J.; Ryum, N. Scandium in aluminium alloys. *Int. Mater. Rev.* **2005**, *50*, 19–44. [[CrossRef](#)]
16. Li, Q.L.; Zhang, Y.S.; Lan, Y.F.; Pei, R.J.; Feng, X.Y.; Xia, T.D.; Liu, D.X. Effect of scandium addition on microstructure and mechanical properties of as-cast Al-5%Cu alloys. *Vacuum* **2020**, *177*, 109385. [[CrossRef](#)]
17. Davydov, V.G.; Rostova, T.D.; Zakharov, V.V.; Filatov, Y.A.; Yelagin, V.I. Scientific principles of making an alloying addition of scandium to aluminium alloys. *Mater. Sci. Eng. A* **2000**, *280*, 30–36. [[CrossRef](#)]
18. Bramfitt, B.L. The effect of carbide and nitride additions on the heterogeneous nucleation behavior of liquid iron. *Metall. Mater. Trans. B.* **1970**, *1*, 1987–1995. [[CrossRef](#)]
19. Chen, X.Y.; Li, Q.A.; Chen, J.; Zhu, L.M. Microstructure and mechanical properties of Mg-Gd-Y-Sm-Al alloy and analysis of grain refinement and strengthening mechanism. *J. Rare Earth* **2019**, *37*, 1351–1358. [[CrossRef](#)]
20. Shiran, M.K.G.; Khalaj, G.; Pouraliakba, H.; Jandaghi, M.R.; Dehnavi, A.S.; Bakhtiari, H. Multilayer Cu/Al/Cu explosive welded joints: Characterizing heat treatment effect on the interface microstructure and mechanical properties. *J. Manuf. Process.* **2018**, *35*, 657–663. [[CrossRef](#)]
21. Jandaghi, M.R.; Saboori, A.; Khalaj, G.; Shiran, M.K.G. Microstructural Evolutions and its Impact on the Corrosion Behaviour of Explosively Welded Al/Cu Bimetal. *Metals* **2020**, *10*, 634. [[CrossRef](#)]
22. Zhang, X.; Wang, Z.H.; Zhou, Z.H.; Xu, J.M. Influence of Rare Earth (Ce and La) Addition on the Performance of Al-3.0 wt%Mg Alloy. *J. Wuhan Univ. Technol.* **2017**, *32*, 611–618. [[CrossRef](#)]
23. Elia, F.D.; Ravindran, C.; Sediako, D.; Kainer, K.U.; Hort, N. Hot tearing mechanisms of B206 aluminum-copper alloy. *Mater. Des.* **2014**, *64*, 44–55.
24. Vlasceanu, M.S.; Lun, S.; Elsayed, A.; Ravindran, C. Effect of Al-5Ti-1B on grain refinement, dendrite coherency and porosity of AZ91E magnesium alloy. *Int. J. Cast Met. Res.* **2015**, *28*, 39–46. [[CrossRef](#)]
25. Tian, L.; Anderson, I.; Riedemann, T.; Russell, A. Modeling the electrical resistivity of deformation processed metal-metal composites. *Acta Mater.* **2014**, *77*, 151–161. [[CrossRef](#)]
26. Qin, R.; Yan, R.F.; Guan, Z.P.; Zhang, G.Q.; Song, J.W.; Ren, M.W.; Wang, J.G. Effect of vanadium on Fe-rich phase, mechanical properties and thermal conductivity of hypoeutectic Al-Si alloy. *Mater. Res. Express* **2021**, *8*, 026518. [[CrossRef](#)]
27. Vandersluis, E.; Ravindran, C. The Role of Porosity in Reducing the Thermal Conductivity of B319 Al Alloy with Decreasing Solidification Rate. *JOM* **2019**, *71*, 2072–2077. [[CrossRef](#)]
28. Zhang, C.; Du, Y.; Liu, S.H.; Liu, Y.L.; Sundman, B. Thermal conductivity of Al-Cu-Mg-Si alloys: Experimental measurement and CALPHAD modeling. *Thermochim. Acta* **2016**, *635*, 8–16. [[CrossRef](#)]
29. Jandaghi, M.R.; Pouraliakbar, H. Elucidating the microscopic origin of electrochemical corrosion and electrical conductivity by lattice response to severe plastic deformation in Al-Mn-Si alloy. *Mater. Res. Bull.* **2018**, *108*, 195–206. [[CrossRef](#)]
30. Perdew, J.P.; Burke, K.; Ernzerhof, M. Generalized Gradient Approximation Made Simple. *Phys. Rev. Lett.* **1996**, *77*, 3865–3868. [[CrossRef](#)]
31. Vanderbilt, D. Soft self-consistent pseudopotentials in a generalized eigenvalue formalism. *Phys. Rev. B* **1990**, *41*, 7892–7895. [[CrossRef](#)] [[PubMed](#)]
32. Pan, Y.; Pu, D.L.; Liu, G.H. Influence of Mo concentration on the structure, mechanical and thermodynamic properties of Mo-Al compounds from first-principles calculations. *Vacuum* **2020**, *175*, 109291. [[CrossRef](#)]
33. Khan, M.I.; Arshad, H.; Rizwan, M.; Gillani, S.S.A.; Shakil, M.; Ahmed, S.; Shakil, M. Investigation of structural, electronic, magnetic and mechanical properties of a new series of equiatomic quaternary Heusler alloys CoYCrZ (Z = Si, Ge, Ga, Al): A DFT study. *J. Alloys Compd.* **2020**, *819*, 152964. [[CrossRef](#)]
34. Mohri, T.; Ying, C.; Kohyama, M.; Ogata, S.; Saengdeejing, A.; Bhattacharya, K.S.; Wakeda, M.; Shinzato, S.; Kimizuka, H. Mechanical properties of Fe-rich Si alloy from Hamiltonian. *npj Comput. Mater.* **2017**, *3*, 100–106. [[CrossRef](#)]
35. Pugh, S.F. XCII. Relations between the elastic moduli and the plastic properties of polycrystalline pure metals. *Philos. Mag.* **1954**, *45*, 823–843. [[CrossRef](#)]